ATLAS CONF Note

ATLAS-CONF-2024-003

March 21, 2024

Search for pair production of boosted Higgs bosons via vector-boson fusion production in the $b\bar{b}b\bar{b}$ final state using pp collisions at $\sqrt{s} = 13$ TeV with the ATLAS detector

The ATLAS Collaboration

A search for Higgs boson (H) pair production via vector boson fusion (VBF) is performed in the Lorentz-boosted regime, where a Higgs boson candidate is reconstructed as a single large-radius jet, using 140 fb^{-1} of proton-proton collision data at 13 TeV recorded by the ATLAS detector. Only Higgs boson decays to bottom quark pairs are considered. The search is particularly sensitive to the quartic coupling between two vector bosons and two Higgs bosons relative to its Standard Model prediction, κ_{2V}. This study constrains κ_{2V} to $0.55 < \kappa_{2V} < 1.49$ at 95% confidence level. The value $\kappa_{2V} = 0$ is excluded with a significance of 3.8σ with other H couplings fixed to their SM values. A search for new heavy spin-0 resonances that would mediate VBF Higgs pair production is carried out in the mass range of 1–5 TeV for the first time under multiple model and decay-width assumptions. No significant deviations from the SM hypotheses are observed and exclusion limits at 95% confidence level are derived.

ATLAS-CONF-2024-003
22 March 2024

1 Introduction

The discovery of the 125 GeV Higgs boson (H) [1–4] by the ATLAS [5] and CMS [6] Collaborations at the Large Hadron Collider (LHC) [7] has led to an extensive research program aimed at measuring its properties, including spin and parity [8–11], natural width [9, 12–14], and couplings with other elementary particles [15–17]. All measurements to date are consistent with the predictions from the Standard Model (SM) [18–23]. However, certain properties, such as quartic couplings (g_{HHVV}) with vector bosons ($V = W, Z$) and the trilinear self-coupling of the Higgs boson (λ_{HHH}), remain unmeasured. In the SM, the former are related to the HVV couplings through the relation $g^{\mathrm{SM}}_{HHVV} = g_{HVV}/v$, and the latter is predicted to be $\lambda^{\mathrm{SM}}_{HHH} = m_H^2/2v^2$, where m_H is the Higgs boson mass and v is the vacuum expectation value of the Higgs field. Measuring the compatibility of these relations with the SM predictions will fundamentally deepen our understanding of the Higgs mechanism.

At the LHC, the coupling modifiers $\kappa_{2V} = g_{HHVV}/g^{\mathrm{SM}}_{HHVV}$ and $\kappa_\lambda = \lambda_{HHH}/\lambda^{\mathrm{SM}}_{HHH}$ are studied via the production of Higgs boson pairs (HH production). In the SM, the main nonresonant HH production modes are via the gluon–gluon fusion process (ggF), with a cross-section of $\sigma^{\mathrm{SM}}_{\mathrm{ggF}} = 31.1^{+2.1}_{-7.2}$ fb [24–34], and via the vector boson fusion process (VBF), with a cross-section of $\sigma^{\mathrm{SM}}_{\mathrm{VBF}} = 1.73 \pm 0.04$ fb [35–37]. The VBF production cross-section depends critically on the value of κ_{2V}. For example, a value of $\kappa_{2V} = 0$ leads to a cross-section that is over 15 times the SM prediction. The Higgs bosons produced in non-SM κ_{2V} scenarios are expected to be more energetic and more central in the detector on average [38]. The leading-order Feynman diagrams of the ggF and VBF HH processes are shown in Figures 1(a) to 1(e). In the SM, Figure 1(a) and Figure 1(b) interfere destructively. Other coupling modifiers related to the HVV coupling (κ_V) and top-quark Yukawa coupling (κ_t) involved in these processes are of less interest in this analysis. The ggF HH production is sensitive to κ_λ while the VBF HH production is sensitive to both κ_λ and κ_{2V}. Heavy resonances (X) beyond the SM may contribute to the resonant HH production [39, 40], as exemplified via VBF process in Figure 1(f). The boosted VBF process provides a distinct signature for investigating these resonances, allowing exploration of uncharted phase space. These HH processes were studied with various decay final states by ATLAS and CMS, including $b\bar{b}b\bar{b}$ [41–46], $b\bar{b}\gamma\gamma$ [47–49], $b\bar{b}\tau^+\tau^-$ [50–52], $b\bar{b}WW^*$ [53], $\gamma\gamma WW^*$ [54], WW^*WW^* [55], $b\bar{b}\ell\ell\ell\ell$ [56], $b\bar{b}\ell\ell + E_{\mathrm{T}}^{\mathrm{miss}}$ [57], and their statistical combinations [17, 58, 59]. No significant excess over the SM background was observed. The most stringent observed (expected) 95% confidence level (CL) interval for the κ_{2V} coupling modifier has been found to be $[0.62, 1.41]$ ($[0.66, 1.37]$) by searching for nonresonant pair production of highly energetic Higgs bosons decaying to bottom quarks by the CMS Collaboration [46]. In Ref. [42], resonant VBF HH production in the mass range of 260–1000 GeV is searched for and no deviation from the background-only hypothesis is observed.

This paper reports a search for nonresonant and resonant VBF $HH \to b\bar{b}b\bar{b}$ production using the Run 2 ATLAS proton-proton (pp) collision data sample with an integrated luminosity of 140 fb^{-1}. The search focuses on a Lorentz-boosted topology, where two high-energy Higgs bosons each form a large-radius jet, referred to as a large-R jet. This topology is particularly sensitive to non-SM values of κ_{2V}, and as such one of the goals of this analysis is to constrain κ_{2V}. Assuming the SM branching ratio of 58.2% for $H \to b\bar{b}$ [29, 60], approximately one third of HH events decay into $b\bar{b}b\bar{b}$, making it the most abundant HH final state. A machine learning-based double b-tagging technique [61, 62] uses the information from the large-R jets and their constituents to identify $H \to b\bar{b}$ decays. The VBF signature is characterised by the presence of VBF jets and provides an effective handle for background suppression. VBF jets are defined as two small-R jets with large invariant mass and rapidity separation. To maximise the sensitivity to the κ_{2V} parameter, the nonresonant analysis is combined with the resolved analysis [44] where the four b-quarks

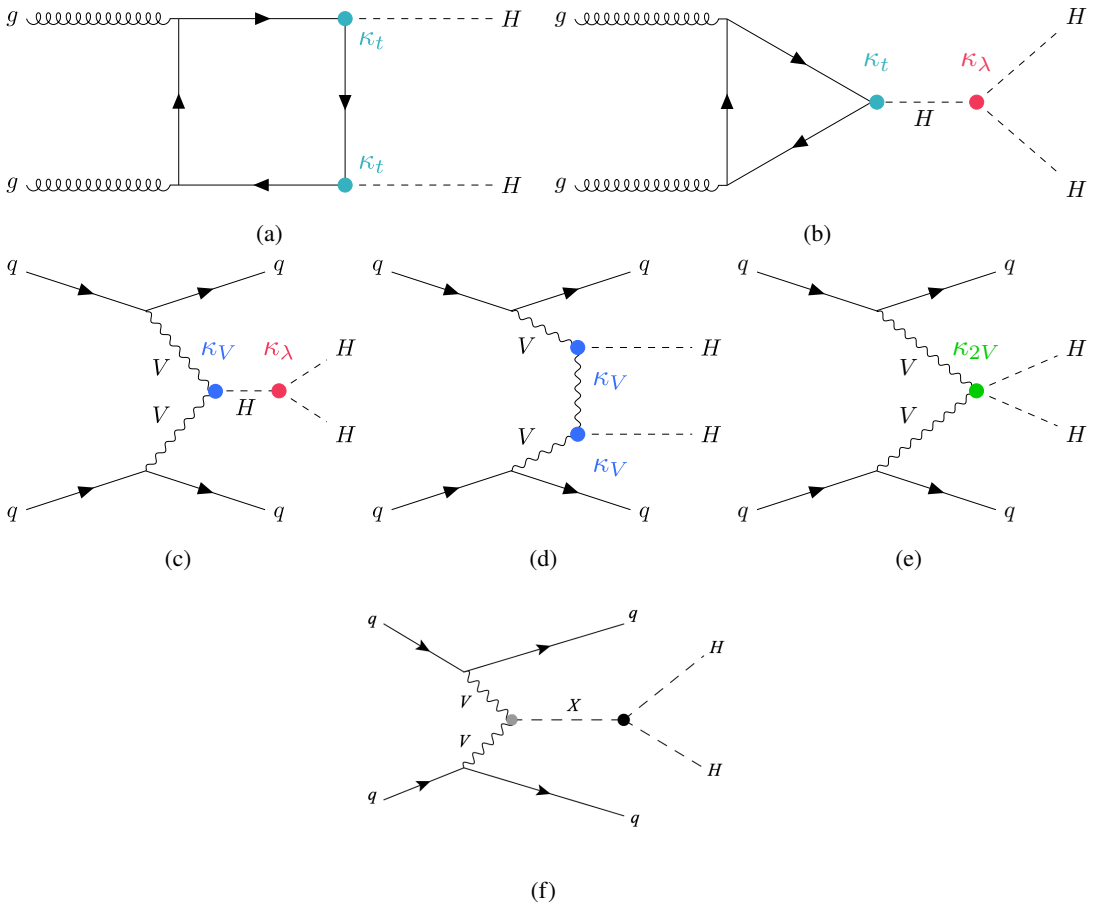

Figure 1: Examples of leading-order Feynman diagrams for Higgs boson pair production. For nonresonant ggF production, diagram (a) involves solely the top-quark Yukawa coupling, while diagram (b) involves the Higgs boson self-coupling. For nonresonant VBF production, diagram (c) involves the self-coupling, diagram (d) involves solely the coupling to vector bosons, and diagram (e) involves the coupling between two Higgs bosons and two vectors bosons. Diagram (f) illustrates the resonant production mode.

are reconstructed as small-R jets. The Higgs bosons considered in the resolved analysis have lower p_{T} compared to those in this boosted search. To avoid double counting events in the boosted nonresonant analysis presented in this paper, events that pass the resolved and boosted analysis selection are removed from the boosted analysis. For the first time, a search for a new heavy spin-0 resonance that would mediate VBF Higgs pair production is carried out in the mass range of 1–5 TeV.

The paper is structured as follows. Section 2 briefly introduces the ATLAS detector. Section 3 details the data and simulation samples used. Section 4 describes the analysis selection. Section 5 explains the background estimate derived from data, and Section 6 covers the multivariate discriminants used. Systematic uncertainties considered in this analysis are detailed in Section 7. Results are provided in Section 8, and conclusions are given in Section 9.

2 The ATLAS experiment

The ATLAS experiment [5] at the LHC is a multipurpose particle detector with a forward–backward symmetric cylindrical geometry and a near 4π coverage in solid angle.[1] It consists of an inner tracking detector surrounded by a thin superconducting solenoid providing a 2 T axial magnetic field, electromagnetic and hadron calorimeters, and a muon spectrometer. The inner tracking detector covers the pseudorapidity range $|\eta| < 2.5$. It consists of silicon pixel, silicon microstrip, and transition radiation tracking detectors. Lead/liquid-argon (LAr) sampling calorimeters provide electromagnetic (EM) energy measurements with high granularity. A steel/scintillator-tile hadron calorimeter covers the central pseudorapidity range ($|\eta| < 1.7$). The endcap and forward regions are instrumented with LAr calorimeters for both the EM and hadronic energy measurements up to $|\eta| = 4.9$. The muon spectrometer surrounds the calorimeters and is based on three large superconducting air-core toroidal magnets with eight coils each. The field integral of the toroids ranges between 2.0 and 6.0 T m across most of the detector. The muon spectrometer includes a system of precision tracking chambers and fast detectors for triggering. A two-level trigger system is used to select events. The first-level trigger is implemented in hardware and uses a subset of the detector information to accept events at a rate below 100 kHz. This is followed by a software-based trigger that reduces the accepted event rate to 1 kHz on average depending on the data-taking conditions. An extensive software suite [63] is used in data simulation, in the reconstruction and analysis of real and simulated data, in detector operations, and in the trigger and data acquisition systems of the experiment.

3 Data and simulation

The analysis is performed using Run 2 ATLAS pp collision data. The average number of interactions per proton bunch crossing (pileup) is between 13 and 38 interactions, depending on the year [64]. After applying ATLAS data quality requirements [65], the dataset corresponds to an integrated luminosity of $140\,\text{fb}^{-1}$. The uncertainty in the integrated luminosity is 0.83% [64], obtained using the LUCID-2 detector [66] for the primary luminosity measurements, complemented by measurements using the inner detector and calorimeters.

Monte Carlo (MC) simulation is used for the modelling of HH processes, top-quark pair production ($t\bar{t}$) and multijet background processes. The $t\bar{t}$ and multijet samples are used solely for event selection optimisation and are identical to those used in Ref. [44]. The final background estimation is obtained through data-driven techniques and described in Section 5. For all HH samples, the Higgs boson mass is fixed to 125 GeV. All samples are processed using the ATLAS simulation framework [67] where the detector response is simulated with GEANT4 [68]. The VBF HH samples are simulated using MADGRAPH 2.7.3 [69] at leading order (LO) with the NNPDF3.0NLO parton distribution function (PDF) set [70]. Samples with coupling modifier values $(\kappa_\lambda, \kappa_{2V}, \kappa_V) = (1, 1, 1)$, $(1, 1.5, 1)$, $(2, 1, 1)$, $(10, 1, 1)$, $(1, 1, 0.5)$, $(-5, 1, 0.5)$, $(0, 1, 1)$, $(1, 0, 1)$, and $(1, 3, 1)$ are explicitly generated and a linear combination [44] of the first six of the listed samples is used to determine the expected yields and distributions for any value of $(\kappa_\lambda, \kappa_{2V}, \kappa_V)$. The method is validated using the remaining simulated samples and good agreement is observed. The SM ggF

[1] ATLAS uses a right-handed coordinate system with its origin at the nominal interaction point in the centre of the detector and the z-axis along the beam pipe. The x-axis points to the centre of the LHC ring, and the y-axis points upward. Cylindrical coordinates (r, ϕ) are used in the transverse plane, ϕ being the azimuthal angle around the z-axis. The pseudorapidity is defined in terms of the polar angle θ as $\eta = -\ln\tan(\theta/2)$. Transverse momentum is defined as $p_\text{T} = p \cdot \sin\theta$. Angular distance is measured in units of $\Delta R \equiv \sqrt{(\Delta\eta)^2 + (\Delta\phi)^2}$.

HH samples are simulated using the POWHEG BOX v2 generator [71–73] at next-to-leading order (NLO), including finite top-quark-mass effects, using the PDF4LHC15 [74] PDF set. A reweighting technique based on the particle-level invariant mass m_{HH} of the Higgs boson pair is applied to the $\kappa_\lambda = 1$ sample to determine the ggF HH yield and kinematic distributions for any value of κ_λ [75]. The ggF HH samples are considered as background processes when constraining κ_{2V} and as signal processes when deriving the results related to κ_λ.

The new heavy spin-0 resonance X that would mediate VBF HH, $pp \to X + jj \to HH + jj$, is simulated using the MADGRAPH5_AMC@NLO 2.6.1 [69] generator at LO in α_S with the NNPDF2.3LO [76] PDF set. The branching ratio of $X \to HH$ is set to 100%. Two resonance-width hypotheses are considered, where the resonance width is denoted as Γ_X: a generic narrow-width signal (Γ_X smaller than the detector resolution of 5–6% of the resonance mass) and a broad-width signal ($\Gamma_X = 20\%$ of the resonance mass) based on the Composite Higgs model [77]. These samples cover a range of resonance masses, denoted as m_X, from 1 TeV to 5 TeV, with increased spacing between the higher mass points and a different number of points between the narrow- and broad-width assumptions. For all resonant and nonresonant HH samples, parton showers and hadronisation are simulated using PYTHIA 8.244 [78] with the A14 set of tuned parameters [79] and the NNPDF2.3LO PDF set [76]. EVTGEN 1.7.0 [80] is used to model the properties of heavy-flavour decays. The pileup modelling is performed by superimposing each simulated hard-scattering event with inelastic pp events generated using PYTHIA 8.186 with the NNPDF2.3LO PDF set and the A3 set of tuned parameters [81], and is weighted to match the observed pileup in data.

4 Event selection

Events must pass large-R jet trigger decisions that require minimum transverse energies of the triggered jet. The threshold varies within the range of 360–420 GeV, depending on the year of data taking [82–84]. Events are required to contain two Higgs boson candidates and two VBF jets. A Higgs boson candidate is reconstructed as a large-R jet using the anti-k_t algorithm [85, 86] with the radius parameter $R = 1.0$, denoted as J. The large-R jets are reconstructed from topological energy depositions [87] in the calorimeter and are trimmed [88, 89] to improve the jet mass resolution and to mitigate the effects of pileup and soft radiation. A method similar to the one used in Ref. [44] is used to correct the four-momentum of large-R jets by accounting for energy lost to soft out-of-cone radiation and to muons and neutrinos in semileptonic b-hadron decays. This correction provides improved jet mass resolution. The mass of a large-R jet (m_J) is calculated using a combination of calorimeter and tracking information [90] to improve the resolution over the whole range of jet p_{T}. The large-R jets must satisfy $250\,\mathrm{GeV} < p_{\mathrm{T}} < 3000\,\mathrm{GeV}$, $|\eta| < 2.0$ and $50\,\mathrm{GeV} < m_J < 600\,\mathrm{GeV}$, corresponding to the region where the jet calibration is valid. The two leading p_{T} large-R jets are considered as the Higgs boson candidates, and the leading jet p_{T} criterion is raised to $p_{\mathrm{T}} > 450\,\mathrm{GeV}$ to ensure that the online trigger is fully efficient. The leading (H_1) and sub-leading (H_2) Higgs boson candidates are ordered by their p_{T}, i.e. $p_{\mathrm{T}}(H_1) \geq p_{\mathrm{T}}(H_2)$. A double b-tagging algorithm based on a deep neural network [61, 62] is applied to the large-R jets to identify $H \to b\bar{b}$ decays. Events with two Higgs boson candidates satisfying the 60% efficiency working point are referred to as 2PASS events. This working point reduces multijet (top-quark) events by a factor of 92 (31). Events with only one Higgs boson candidate satisfying the 60% efficiency working point are referred to as 1PASS and are used for background estimation. The small-R jets, denoted as j, are reconstructed from particle-flow objects [91] using an $R = 0.4$ anti-k_t algorithm. They must have $p_{\mathrm{T}} > 20\,\mathrm{GeV}$ and $|\eta| < 4.5$, and those with $p_{\mathrm{T}} < 60\,\mathrm{GeV}$ and $|\eta| < 2.4$ must satisfy a requirement based on the output of the multivariate jet vertex tagger algorithm [92] to reduce the effect from pileup. The jet energy (E) is corrected by applying

in situ corrections for the contributions from pileup events [93]. To remove overlap with the Higgs boson candidates, the distance between a small-R jet and the selected Higgs boson candidates must satisfy $\Delta R(J, j) > 1.4$. The two leading p_{T} small-R jets are assigned as VBF jets and required to satisfy the criteria $|\Delta\eta(j, j)| > 3$ and $m_{jj} > 1\,\mathrm{TeV}$.

After the preselections described above, 1Pass and 2Pass events are separately classified into signal regions (SRs), validation regions (VRs), and control regions (CRs) according to the following criteria defined in the m_{H_1}–m_{H_2} plane. Events in the SR reside in the region defined by

$$\sqrt{\left(\frac{m_{H_1} - 124\,\mathrm{GeV}}{1500\,\mathrm{GeV}/m_{H_1}}\right)^2 + \left(\frac{m_{H_2} - 117\,\mathrm{GeV}}{1900\,\mathrm{GeV}/m_{H_2}}\right)^2} < 1.6\,\mathrm{GeV}. \tag{1}$$

Events in the VR reside in the region bounded by the SR boundary and

$$\sqrt{\left(\frac{m_{H_1} - 124\,\mathrm{GeV}}{0.1\ln(m_{H_1}/\mathrm{GeV})}\right)^2 + \left(\frac{m_{H_2} - 117\,\mathrm{GeV}}{0.1\ln(m_{H_2}/\mathrm{GeV})}\right)^2} < 100\,\mathrm{GeV}, \tag{2}$$

and events in the CR reside in the region bounded by the VR outer boundary and

$$\sqrt{\left(\frac{m_{H_1} - 124\,\mathrm{GeV}}{0.1\ln(m_{H_1}/\mathrm{GeV})}\right)^2 + \left(\frac{m_{H_2} - 117\,\mathrm{GeV}}{0.1\ln(m_{H_2}/\mathrm{GeV})}\right)^2} < 170\,\mathrm{GeV}. \tag{3}$$

The values of 124 GeV and 117 GeV in Equations (1) to (3) are chosen such that they correspond to the centres of the m_{H_1} and m_{H_2} distributions of the VBF HH events from simulation. These centres deviate from the measured Higgs boson mass of 125 GeV due to detector effects, as well as energy lost to neutrinos from the b-hadron decays and to out-of-cone radiation. The variables m_{H_1} and m_{H_2} in these equations are in units of GeV. The SR definition is optimised to maximise the overall $S/\sqrt{B}$. The signal S is the yield of $\kappa_{2V} = 0$ VBF HH events in simulation which is chosen to maximise the sensitivity to the κ_{2V} coupling as it is a representative proxy for non-SM κ_{2V} samples. The background B is the expected number of background events estimated using the $t\bar{t}$ and multijet simulated samples. As multijet background processes preferentially populate the m_{H_1}–m_{H_2} plane in the lower Higgs boson candidate mass region compared to HH processes, Equations (2) and (3) help reduce contributions from multijet events. The boundaries of the SR, VR, and CR in the reconstructed m_{H_1}–m_{H_2} plane are shown in Figure 2 for the 1Pass and 2Pass selections of the analysis. The m_{H_1}–m_{H_2} plane is smoothly falling across the Higgs boson candidate masses. The majority of HH events are captured by the signal region boundary; the fraction of 2Pass events in the SR is 76% (78%–55%) for nonresonant (resonant 1 TeV–5 TeV) events. The overall signal acceptance times efficiency in the 2Pass SR ranges from 1% for a representative nonresonant non-SM signal sample to 0.02% for the SM nonresonant signal sample. For the resonant signal samples, the overall acceptance times efficiency ranges from 5% to 10%, depending on the mass and width of the resonance.

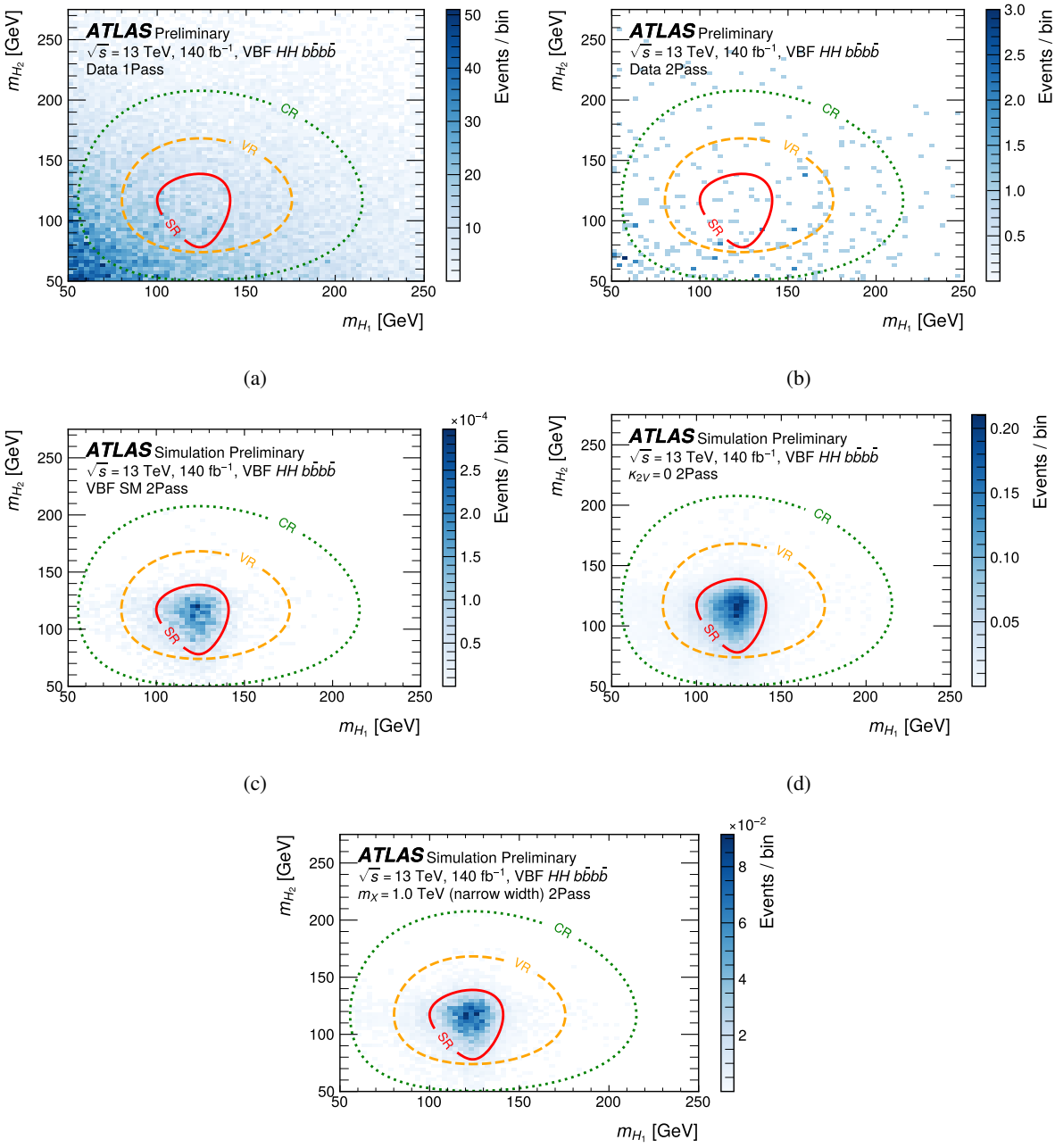

Figure 2: The mass planes of the reconstructed Higgs boson candidates for the (a) 1Pass and (b) 2Pass selections of the analysis, shown for the data events. The mass planes for the 2Pass selection of the analysis are shown for the (c) VBF SM $\kappa_{2V} = 1$ HH, (d) VBF $\kappa_{2V} = 0$ HH, and (e) $m_X = 1$ TeV spin-0 narrow-width resonance HH samples. The continuous red line describes the Signal Region (SR). The Validation Region (VR) lies between the dashed yellow line and the continuous red line. The Control Region (CR) lies between the dotted green line and the dashed yellow line.

5 Background estimation

Background processes in the SR predominantly originate from nonresonant multijet production of multiple heavy (b/t) quarks and from jets initiated by non-heavy quarks misidentified as originating from heavy quarks. The background contribution coming from single-Higgs and diboson events were found to be negligible. The multijet background, which is comprised of approximately 10% $t\bar{t}$ events, is estimated using a data-driven method and 1Pass events. The signal contamination in the 1Pass selection is at most 1% depending on the signal considered. It increases to up to 8% in the most signal-like bin of the final discriminant (described in Section 6), which is below the statistical uncertainty of this bin. As the difference between the shape of the final discriminant in 1Pass and 2Pass events is within statistical uncertainty, an inclusive normalisation factor is derived from the CR and applied to the SR. The normalisation factor w is derived by calculating the ratio between the number of events in the CR 2Pass and CR 1Pass:

$$w = 0.0081 \pm 0.0010. \tag{4}$$

The uncertainty is obtained by re-deriving this ratio in the VR and computing the difference between the value of w derived in the CR and the VR. The background estimate in the 2Pass SR is thus obtained by multiplying the relevant distribution in the 1Pass SR by w. Alternative definitions for the CR and VR boundaries, which split the nominal definitions of CR and VR into quadrants, are found to yield values of w that are consistent with the nominal estimate. To cover any potential residual shape differences, a shape uncertainty on the final discriminant is estimated by taking the relative difference between the 1Pass and 2Pass discriminant distributions in the VR and symmetrising around the background estimate.

6 Multivariate Discriminants

Boosted decision trees (BDTs) implemented in the XGBoost [94] library are used to separate signal events from background events in the SR. In both the nonresonant and resonant analyses, orthogonality between training, testing, and validation samples is ensured by splitting the available data by event number. Hyperparameters are optimised using the validation samples to enhance the classifier's performance, and the kinematic variables used as input are listed in Table 1. In the nonresonant analysis, a BDT is trained to separate $\kappa_{2V} = 0$ signal events from background events consisting of the nonresonant multijet background estimate and SM ggF and VBF HH production events. The $\kappa_{2V} = 0$ signal is chosen as a representative proxy for non-SM values of κ_{2V}, allowing to maximise the sensitivity to the κ_{2V} coupling.

The resonant analysis uses a mass-parametrised BDT (pBDT) in order to accommodate multiple resonant signals with different mass hypotheses, inspired by parametrised neural networks [95]. In addition to the variables listed in Table 1, the pBDT includes the truth mass of the heavy resonances as an additional input parameter. Signals are composed of thirteen narrow width MC samples with distinct hypotheses for the truth mass of the heavy resonance. The broad width samples are not used during training. The background is taken from the background estimated in Section 5. A random value from the available signal true resonance masses m_X is assigned to each background event in the training. To ensure an adequate number of training statistics, the requirements on the VBF jets are removed and the double b-tagging working point requirements are relaxed to the 70% efficiency working point during training for the resonant analysis. The nominal selection is reinstated after training.

Table 1: Kinematic variables used in the BDT training in both the nonresonant and resonant analyses. Additionally, the truth mass of the resonance is used as an input variable in the resonant analysis.

Relevant Objects	Kinematics used in training
Higgs Boson Candidate (H_i, $i = 1, 2$)	$p_{\mathrm{T}}^{H_i}$, η_{H_i}
Di-Higgs System (HH)	p_{T}^{HH}, η_{HH}, m_{HH}
VBF Jets (j_i, $i = 1, 2$)	$p_{\mathrm{T}}^{j_i}$, η_{j_i}, E_{j_i}

7 Systematic uncertainties

Although the analysis is limited by the statistical uncertainty, systematic uncertainties on the background and signals are evaluated. Both a normalisation and shape uncertainty are assigned to the data-driven background estimate, as described in Section 5. Uncertainties resulting from detector effects only affect signal simulation. The impact of the main sources of uncertainty on the signal yield are evaluated for various hypothesised signals. The dominant systematic uncertainty in this analysis stems from the double b-tagging algorithm (20–30%). It is derived in four p_{T}^{J} bins using a $Z \to b\bar{b}$ control sample [62]. As this $Z \to b\bar{b}$ control sample is statistically limited, the systematic uncertainty coming from the double b-tagging algorithm is uncorrelated across the four p_{T}^{J} bins while correlated between the two large-R jets in each event. The uncertainty in the integrated luminosity is 0.83% and in the pileup modelling is < 0.1%. Uncertainties affecting the final state reconstruction and identification include the energy and mass scales of the large-R jets (1–10%), the large-R jet energy resolution and mass resolution (< 1%) [96, 97], the small-R jet energy scale and resolution (1–10%) [93, 98]. The efficiency and acceptance of nonresonant and resonant signals are also affected by theoretical modelling uncertainties, such as the parton showering (5–10%) and renormalisation and factorisation scale choices (1–5%). Theoretical uncertainties on the $H \to b\bar{b}$ branching ratio (3.5%) [29] are included. Theoretical uncertainties on the nonresonant ggF and VBF HH cross-sections arising from uncertainties on the PDF and α_{s}, as well as the choice of renormalisation scheme and the scale of the top-quark mass, are taken from Refs. [29, 30, 34]. No theoretical uncertainties on the resonant HH cross-sections are considered.

8 Results

A binned maximum likelihood fit to the BDT distributions in the 2Pass SR is carried out with the systematic uncertainties parametrised as nuisance parameters. The BDT output binning transformation is the same as the one detailed in Ref. [99]. The observed BDT distribution of data, as well as the background-only fit to the distribution, is presented in Figure 3. Good agreement is found between the data and the background-only hypothesis. No data are observed in the most signal-like bin while the expectation from background contribution before the fit is 1.1 ± 0.1 events. In the nonresonant search, a combination with the ggF and VBF categories of the resolved analysis [44] is additionally performed to improve the sensitivity to κ_{2V}. Uncertainties stemming from common sources in both analyses are correlated. The values of twice the negative-logarithm of the profile likelihood ratio ($-2\ln\Lambda$) as a function of κ_{2V} are shown in Figure 4 for the resolved and boosted analyses, and their combination. The best-fit κ_{2V} value obtained from the fit to the data is $1.01^{+0.24}_{-0.23}$ for the boosted result and $1.01^{+0.23}_{-0.22}$ for the combined result. The boosted result provides an observed (expected) constraint of $0.52 < \kappa_{2V} < 1.52$ ($0.32 < \kappa_{2V} < 1.71$) at 95% CL.

The combined observed (expected) constraints obtained are $0.55 < \kappa_{2V} < 1.49$ ($0.37 < \kappa_{2V} < 1.67$) at 95% CL. The Higgs coupling $\kappa_{2V} = 0$ is excluded with an observed (expected) significance of 3.4σ (2.9σ). When combining the boosted and resolved results, the Higgs coupling $\kappa_{2V} = 0$ is excluded with an observed (expected) significance of 3.8σ (3.3σ). These results are obtained assuming κ_λ and all other couplings values are as predicted by the SM. The exclusion constraints in the two-dimensional κ_λ–κ_{2V} coupling modifier space are presented in Figure 5. The resolved and boosted analyses are sensitive to complementary coupling parameters; the κ_λ sensitivity is driven by the resolved analysis, while the κ_{2V} sensitivity is dominated by the boosted analysis.

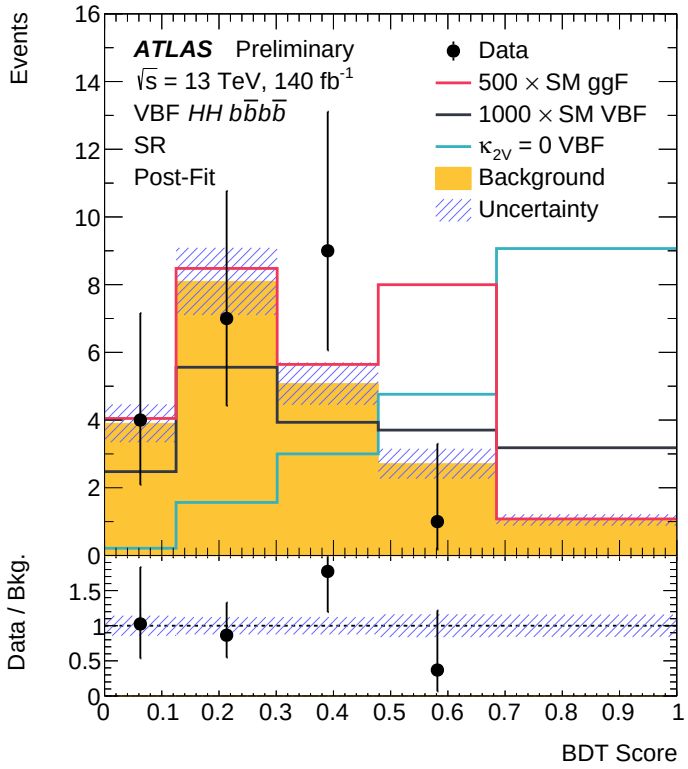

Figure 3: The distributions of the BDT response used in the nonresonant analysis after a background-only fit to the data in the signal region. The SM ggF sample, SM VBF sample, and $\kappa_{2V} = 0$ VBF sample are shown. The lower panel shows the ratio of data to the total background prediction, with its uncertainty represented by the shaded band. The error bars on the data points represent the statistical uncertainty.

Upper limits on the cross-section for the narrow and broad width resonance assumptions are set in each available signal hypothesis using the asymptotic formula [100] based on the CL_s method [101]. The results are shown in Figure 6 for narrow and broad width resonances, which have masses in the range $1\,\text{TeV} \leq m_X \leq 5\,\text{TeV}$ and $1.2\,\text{TeV} \leq m_X \leq 2\,\text{TeV}$, respectively. The loss in sensitivity at high mass values is attributed to the smaller efficiency of the double b-tagging algorithm in the highly boosted regime. The observed limits at 1.6 TeV (1.8 TeV) and above drop for the narrow (broad) width resonance since no data are observed in the most signal-like bin of these high mass pBDT distributions. In the narrow-width assumption, the observed (expected) limit range spans from 4.6 fb (3.1 fb) for $m_X = 1\,\text{TeV}$ to 1.9 fb (3.0 fb) for $m_X = 5\,\text{TeV}$ and extends to 0.7 fb (1.2 fb) for $m_X = 1.8\,\text{TeV}$. In the broad-width assumption, the observed (expected) limit range decreases from 2.5 fb (2.1 fb) for $m_X = 1.2\,\text{TeV}$ to 0.8 fb (1.3 fb) for $m_X = 2\,\text{TeV}$.

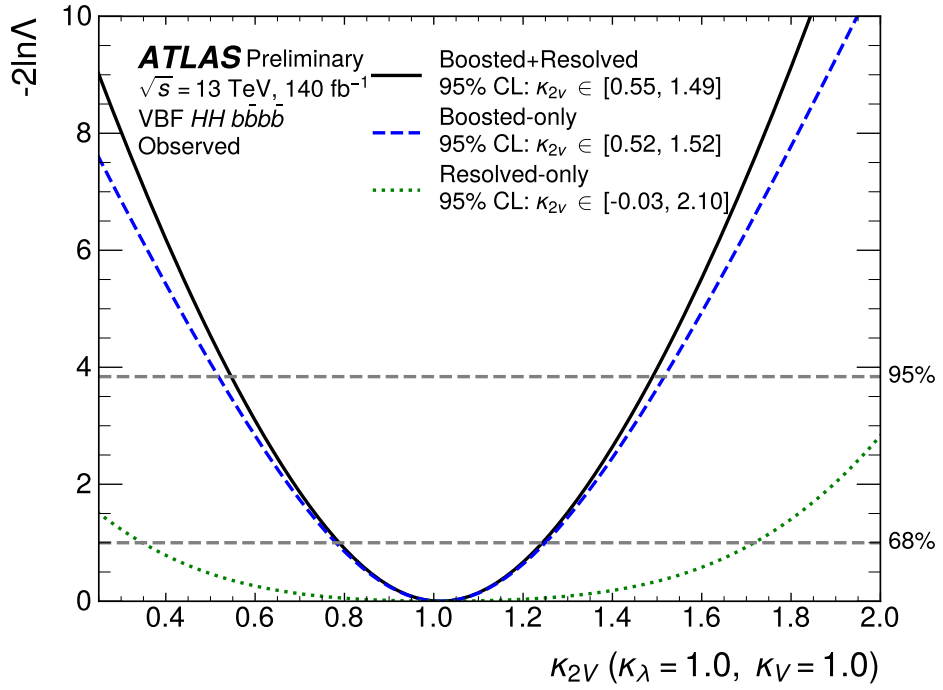

(a)

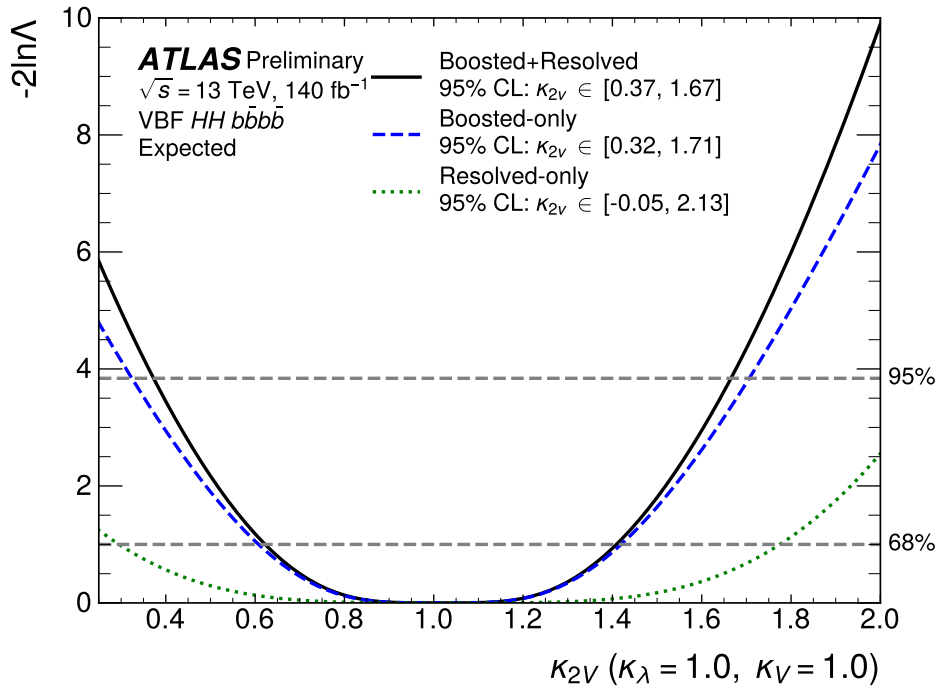

(b)

Figure 4: Observed (a) and expected (b) values of $-2\ln\Lambda$ as a function of κ_{2V} for the resolved (dotted green) and boosted (dashed blue) analyses, and their combination (solid black), with all other coupling modifiers fixed to their SM predictions.

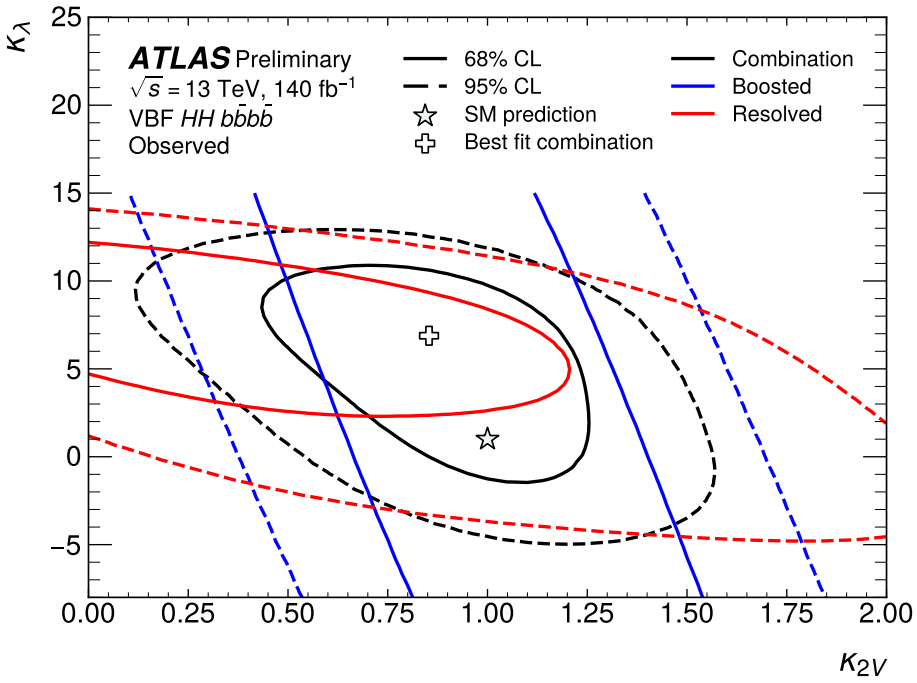

(a)

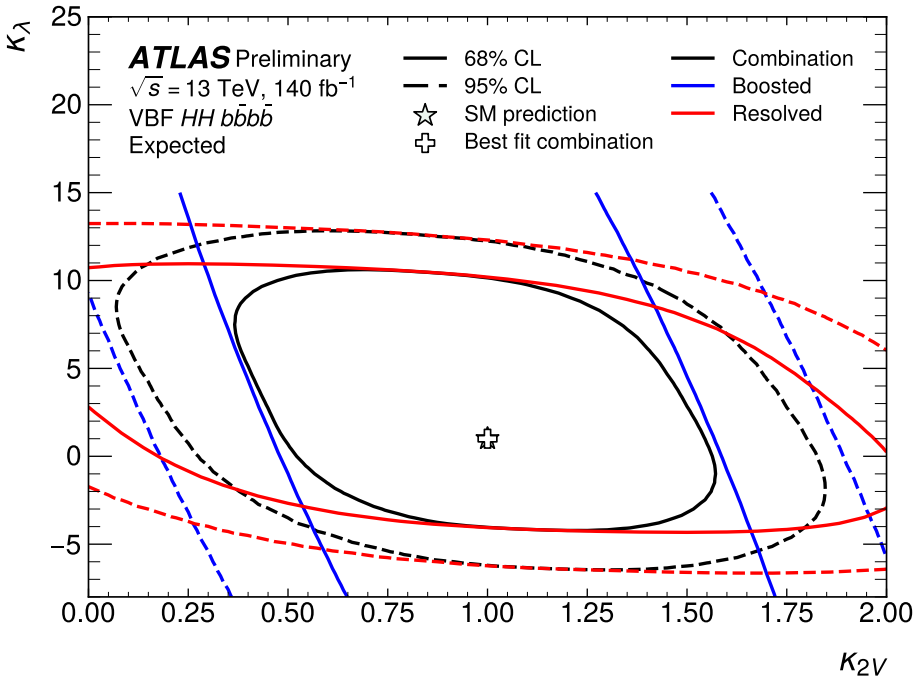

(b)

Figure 5: Observed (a) and expected (b) likelihood contours at 68% (solid line) and 95% (dashed line) CL in the κ_λ–κ_{2V} plane. The red, blue, and black colors represent the resolved-only, boosted-only, and boosted+resolved combination results, respectively. All other coupling modifiers are fixed to their SM predictions. The SM prediction is indicated by the star, while the best-fit value is denoted by the cross. The shift in the observed value from the SM prediction is driven by the resolved analysis. The observed constraint Higgs combination for κ_λ values is less stringent than that for the resolved-only fit due to the different best-fit values of the κ_{2V} modifier. The result for κ_λ values above 15 is not plotted for clarity.

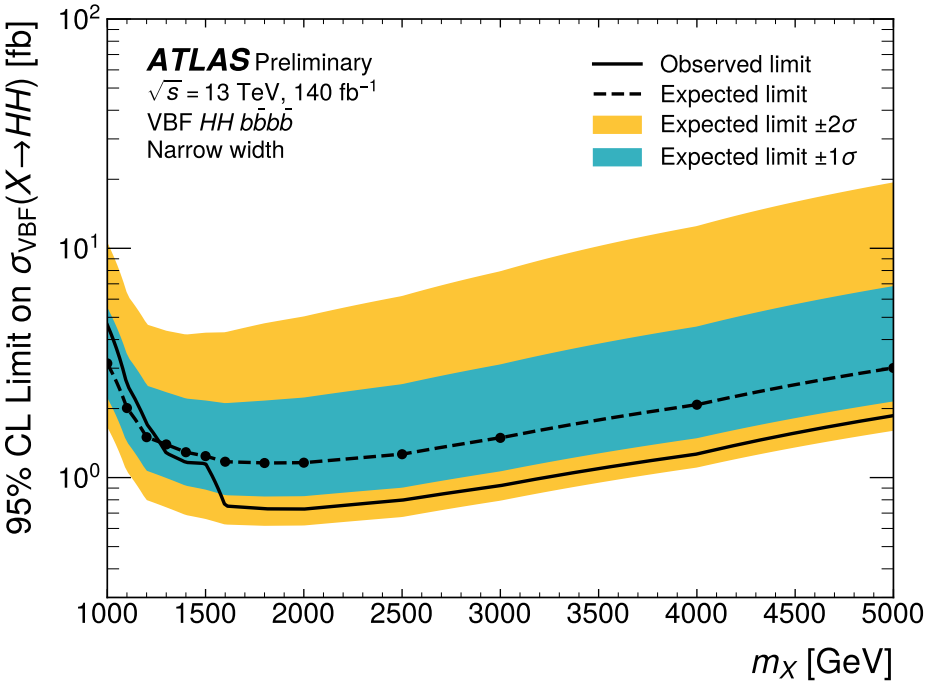

(a)

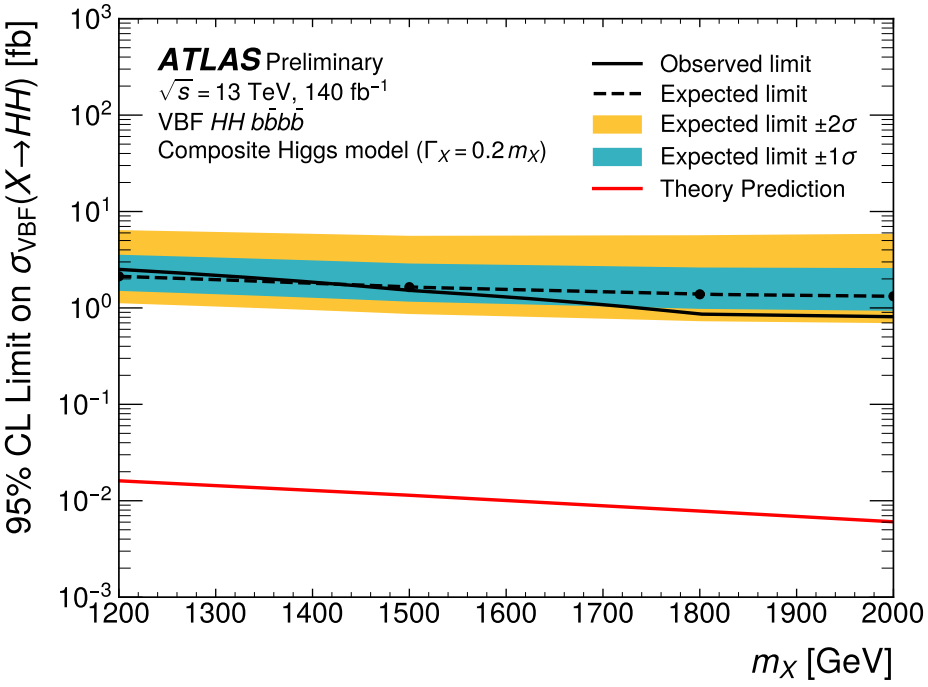

(b)

Figure 6: Expected (dashed black lines) and observed (solid black lines) 95% CL upper limits on the cross-section of spin-0 heavy resonances with (a) narrow width and (b) broad width assumptions. The SM $H \to b\bar{b}$ branching ratio is assumed in both cases. The $\pm 1\sigma$ and $\pm 2\sigma$ uncertainty ranges for the expected limits are shown as coloured bands. The theoretical prediction for the Composite Higgs model calculated at leading order [77] under the $\Gamma_X/m_X = 20\%$ assumption is shown as the solid red line.

9 Conclusion

A search for the production of Higgs boson pairs via VBF production in the four b-quark final state is presented. The analysis focuses on the Lorentz-boosted regime where each Higgs boson is reconstructed as a large-R jet. This regime yields particular sensitivity to anomalous κ_{2V} values which give rise to energetic Higgs bosons. A machine learning-based double b-tagging technique is employed to enhance analysis sensitivity. The data are found to agree with the background-only hypothesis. The observed (expected) constraints obtained are $0.55 < \kappa_{2V} < 1.49$ ($0.37 < \kappa_{2V} < 1.67$) at 95% CL. The allowed 95% CL for κ_{2V} is reduced by a factor of two compared to previous ATLAS publications [44]. The Higgs coupling $\kappa_{2V} = 0$ is excluded with an observed (expected) significance of 3.8σ (3.3σ). A search is also performed for a new heavy spin-0 resonance that would mediate VBF HH in a mass range between 1 TeV and 5 TeV for the first time. No significant excess is observed and exclusion limits are set on the production cross-section.

References

[1] ATLAS Collaboration, *Observation of a new particle in the search for the Standard Model Higgs boson with the ATLAS detector at the LHC*, Phys. Lett. B **716** (2012) 1, arXiv: 1207.7214 [hep-ex] (cit. on p. 2).

[2] CMS Collaboration, *Observation of a new boson at a mass of 125 GeV with the CMS experiment at the LHC*, Phys. Lett. B **716** (2012) 30, arXiv: 1207.7235 [hep-ex] (cit. on p. 2).

[3] ATLAS Collaboration, *Observation of $H \to b\bar{b}$ decays and VH production with the ATLAS detector*, Phys. Lett. B **786** (2018) 59, arXiv: 1808.08238 [hep-ex] (cit. on p. 2).

[4] CMS Collaboration, *Observation of Higgs Boson Decay to Bottom Quarks*, Phys. Rev. Lett. **121** (2018) 121801, arXiv: 1808.08242 [hep-ex] (cit. on p. 2).

[5] ATLAS Collaboration, *The ATLAS Experiment at the CERN Large Hadron Collider*, JINST **3** (2008) S08003 (cit. on pp. 2, 4).

[6] CMS Collaboration, *The CMS experiment at the CERN LHC*, JINST **3** (2008) S08004 (cit. on p. 2).

[7] L. Evans and P. Bryant, *LHC Machine*, JINST **3** (2008) S08001 (cit. on p. 2).

[8] ATLAS Collaboration, *Study of the spin and parity of the Higgs boson in diboson decays with the ATLAS detector*, Eur. Phys. J. C **75** (2015) 476, arXiv: 1506.05669 [hep-ex], Erratum: Eur. Phys. J. C **76** (2016) 152 (cit. on p. 2).

[9] CMS Collaboration, *Constraints on the spin-parity and anomalous HVV couplings of the Higgs boson in proton collisions at 7 and 8 TeV*, Phys. Rev. D **92** (2015) 012004, arXiv: 1411.3441 [hep-ex] (cit. on p. 2).

[10] ATLAS Collaboration, *CP Properties of Higgs Boson Interactions with Top Quarks in the $t\bar{t}H$ and tH Processes Using $H \to \gamma\gamma$ with the ATLAS Detector*, Phys. Rev. Lett. **125** (2020) 061802, arXiv: 2004.04545 [hep-ex] (cit. on p. 2).

[11] CMS Collaboration,
Study of the Mass and Spin-Parity of the Higgs Boson Candidate Via Its Decays to Z Boson Pairs,
Phys. Rev. Lett. **110** (2013) 081803, arXiv: 1212.6639 [hep-ex] (cit. on p. 2).

[12] ATLAS Collaboration, *Constraints on the off-shell Higgs boson signal strength in the high-mass ZZ and WW final states with the ATLAS detector*, Eur. Phys. J. C **75** (2015) 335,
arXiv: 1503.01060 [hep-ex] (cit. on p. 2).

[13] CMS Collaboration, *Search for Higgs boson off-shell production in proton–proton collisions at 7 and 8 TeV and derivation of constraints on its total decay width*, JHEP **09** (2016) 051,
arXiv: 1605.02329 [hep-ex] (cit. on p. 2).

[14] CMS Collaboration,
Limits on the Higgs boson lifetime and width from its decay to four charged leptons,
Phys. Rev. D **92** (2015) 072010, arXiv: 1507.06656 [hep-ex] (cit. on p. 2).

[15] ATLAS and CMS Collaborations,
Measurements of the Higgs boson production and decay rates and constraints on its couplings from a combined ATLAS and CMS analysis of the LHC pp collision data at $\sqrt{s} = 7$ and 8 TeV,
JHEP **08** (2016) 045, arXiv: 1606.02266 [hep-ex] (cit. on p. 2).

[16] ATLAS Collaboration,
A detailed map of Higgs boson interactions by the ATLAS experiment ten years after the discovery,
Nature **607** (2022) 52, arXiv: 2207.00092 [hep-ex] (cit. on p. 2).

[17] CMS Collaboration,
A portrait of the Higgs boson by the CMS experiment ten years after the discovery,
Nature **607** (2022) 60, arXiv: 2207.00043 [hep-ex] (cit. on p. 2).

[18] F. Englert and R. Brout, *Broken Symmetry and the Mass of Gauge Vector Mesons*,
Phys. Rev. Lett. **13** (1964) 321 (cit. on p. 2).

[19] P. W. Higgs, *Broken symmetries, massless particles and gauge fields*, Phys. Lett. **12** (1964) 132
(cit. on p. 2).

[20] P. W. Higgs, *Broken Symmetries and the Masses of Gauge Bosons*, Phys. Rev. Lett. **13** (1964) 508
(cit. on p. 2).

[21] P. W. Higgs, *Spontaneous Symmetry Breakdown without Massless Bosons*,
Phys. Rev. **145** (1966) 1156 (cit. on p. 2).

[22] G. S. Guralnik, C. R. Hagen, and T. W. B. Kibble,
Global Conservation Laws and Massless Particles, Phys. Rev. Lett. **13** (1964) 585 (cit. on p. 2).

[23] T. W. B. Kibble, *Symmetry Breaking in Non-Abelian Gauge Theories*, Phys. Rev. **155** (1967) 1554
(cit. on p. 2).

[24] S. Dawson, S. Dittmaier, and M. Spira,
Neutral Higgs-boson pair production at hadron colliders: QCD corrections,
Phys. Rev. D **58** (1998) 115012, arXiv: hep-ph/9805244 [hep-ph] (cit. on p. 2).

[25] D. Y. Shao, C. S. Li, H. T. Li, and J. Wang,
Threshold resummation effects in Higgs boson pair production at the LHC, JHEP **07** (2013) 169,
arXiv: 1301.1245 [hep-ph] (cit. on p. 2).

[26] D. de Florian and J. Mazzitelli,
Higgs Boson Pair Production at Next-to-Next-to-Leading Order in QCD,
Phys. Rev. Lett. **111** (2013) 201801, arXiv: 1309.6594 [hep-ph] (cit. on p. 2).

[27] D. de Florian and J. Mazzitelli,
Higgs pair production at next-to-next-to-leading logarithmic accuracy at the LHC,
JHEP **09** (2015) 053, arXiv: 1505.07122 [hep-ph] (cit. on p. 2).

[28] S. Borowka et al., *Higgs Boson Pair Production in Gluon Fusion at Next-to-Leading Order with Full Top-Quark Mass Dependence*,
Phys. Rev. Lett. **117** (2016) 012001, [Erratum: Phys. Rev. Lett. **1**17 (2016) 079901],
arXiv: 1604.06447 [hep-ph] (cit. on p. 2).

[29] LHC Higgs Cross Section Working Group,
Handbook of LHC Higgs Cross Sections: 4. Deciphering the Nature of the Higgs Sector,
CERN-2017-002-M (2017), arXiv: 1610.07922 [hep-ph] (cit. on pp. 2, 9).

[30] M. Grazzini et al., *Higgs boson pair production at NNLO with top quark mass effects*,
JHEP **05** (2018) 059, arXiv: 1803.02463 [hep-ph] (cit. on pp. 2, 9).

[31] R. Bonciani, G. Degrassi, P. P. Giardino, and R. Gröber,
Analytical Method for Next-to-Leading-Order QCD Corrections to Double-Higgs Production,
Phys. Rev. Lett. **121** (2018) 162003, arXiv: 1806.11564 [hep-ph] (cit. on p. 2).

[32] J. Baglio et al., *Gluon fusion into Higgs pairs at NLO QCD and the top mass scheme*,
Eur. Phys. J. C **79** (2019) 459, arXiv: 1811.05692 [hep-ph] (cit. on p. 2).

[33] G. Heinrich, S. P. Jones, M. Kerner, G. Luisoni, and L. Scyboz, *Probing the trilinear Higgs boson coupling in di-Higgs production at NLO QCD including parton shower effects*,
JHEP **06** (2019) 066, arXiv: 1903.08137 [hep-ph] (cit. on p. 2).

[34] J. Baglio et al., $gg \to HH$*: Combined uncertainties*, Phys. Rev. D **103** (2021) 056002,
arXiv: 2008.11626 (cit. on pp. 2, 9).

[35] J. Baglio et al., *The measurement of the Higgs self-coupling at the LHC: theoretical status*,
JHEP **04** (2013) 151, arXiv: 1212.5581 (cit. on p. 2).

[36] L.-S. Ling et al.,
NNLO QCD corrections to Higgs pair production via vector boson fusion at hadron colliders,
Phys. Rev. D **89** (2014) 073001, arXiv: 1401.7754 (cit. on p. 2).

[37] F. A. Dreyer and A. Karlberg, *Vector-boson fusion Higgs pair production at* $\mathrm{N^3LO}$,
Phys. Rev. D **98** (11 2018) 114016, arXiv: 1811.07906 (cit. on p. 2).

[38] F. Bishara, R. Contino, and J. Rojo,
Higgs pair production in vector-boson fusion at the LHC and beyond,
Eur. Phys. J. C **77** (2017) 481, arXiv: 1611.03860 [hep-ph] (cit. on p. 2).

[39] G. Branco et al., *Theory and phenomenology of two-Higgs-doublet models*,
Phys. Rept. **516** (2012) 1, arXiv: 1106.0034 [hep-ph] (cit. on p. 2).

[40] R. K. Barman, C. Englert, D. Gonçalves, and M. Spannowsky,
Di-Higgs resonance searches in weak boson fusion, Phys. Rev. D **102** (2020) 055014,
arXiv: 2007.07295 [hep-ph] (cit. on p. 2).

[41] ATLAS Collaboration, *Search for pair production of Higgs bosons in the* $b\bar{b}b\bar{b}$ *final state using proton–proton collisions at* $\sqrt{s} = 13$ *TeV with the ATLAS detector*, JHEP **01** (2019) 030,
arXiv: 1804.06174 [hep-ex] (cit. on p. 2).

[42] ATLAS Collaboration, *Search for the* $HH \to b\bar{b}b\bar{b}$ *process via vector-boson fusion production using proton–proton collisions at* $\sqrt{s} = 13$ *TeV with the ATLAS detector*, JHEP **07** (2020) 108,
arXiv: 2001.05178 [hep-ex] (cit. on p. 2), Erratum: JHEP **01** (2021) 145.

[43] ATLAS Collaboration, *Search for resonant pair production of Higgs bosons in the $b\bar{b}b\bar{b}$ final state using pp collisions at $\sqrt{s} = 13$ TeV with the ATLAS detector*, Phys. Rev. D **105** (2022) 092002, arXiv: 2202.07288 [hep-ex] (cit. on p. 2).

[44] ATLAS Collaboration, *Search for nonresonant pair production of Higgs bosons in the $b\bar{b}b\bar{b}$ final state in pp collisions at $\sqrt{s} = 13$ TeV with the ATLAS detector*, Phys. Rev. D **108** (2023) 052003, arXiv: 2301.03212 [hep-ex] (cit. on pp. 2, 4, 5, 9, 14).

[45] CMS Collaboration, *Search for Higgs Boson Pair Production in the Four b Quark Final State in Proton–Proton Collisions at $\sqrt{s} = 13$ TeV*, Phys. Rev. Lett. **129** (2022) 081802, arXiv: 2202.09617 [hep-ex] (cit. on p. 2).

[46] CMS Collaboration, *Search for nonresonant pair production of highly energetic Higgs bosons decaying to bottom quarks*, Phys. Rev. Lett. **131** (2023) 041803, arXiv: 2205.06667 [hep-ex] (cit. on p. 2).

[47] ATLAS Collaboration, *Search for Higgs boson pair production in the $\gamma\gamma b\bar{b}$ final state with 13 TeV pp collision data collected by the ATLAS experiment*, JHEP **11** (2018) 040, arXiv: 1807.04873 [hep-ex] (cit. on p. 2).

[48] ATLAS Collaboration, *Search for Higgs boson pair production in the two bottom quarks plus two photons final state in pp collisions at $\sqrt{s} = 13$ TeV with the ATLAS detector*, Phys. Rev. D **106** (2022) 052001, arXiv: 2112.11876 [hep-ex] (cit. on p. 2).

[49] CMS Collaboration, *Search for nonresonant Higgs boson pair production in final states with two bottom quarks and two photons in proton–proton collisions at $\sqrt{s} = 13$ TeV*, JHEP **03** (2021) 257, arXiv: 2011.12373 [hep-ex] (cit. on p. 2).

[50] ATLAS Collaboration, *Search for Resonant and Nonresonant Higgs Boson Pair Production in the $b\bar{b}\tau^+\tau^-$ Decay Channel in pp Collisions at $\sqrt{s} = 13$ TeV with the ATLAS Detector*, Phys. Rev. Lett. **121** (2018) 191801, arXiv: 1808.00336 [hep-ex], Erratum: Phys. Rev. Lett. **122** (2019) 089901 (cit. on p. 2).

[51] ATLAS Collaboration, *Search for resonant and non-resonant Higgs boson pair production in the $b\bar{b}\tau^+\tau^-$ decay channel using 13 TeV pp collision data from the ATLAS detector*, JHEP **07** (2023) 040, arXiv: 2209.10910 [hep-ex] (cit. on p. 2).

[52] CMS Collaboration, *Search for nonresonant Higgs boson pair production in final state with two bottom quarks and two tau leptons in proton–proton collisions at $\sqrt{s} = 13$ TeV*, Phys. Lett. B **842** (2023) 137531, arXiv: 2206.09401 [hep-ex] (cit. on p. 2).

[53] ATLAS Collaboration, *Search for Higgs boson pair production in the $b\bar{b}WW^*$ decay mode at $\sqrt{s} = 13$ TeV with the ATLAS detector*, JHEP **04** (2019) 092, arXiv: 1811.04671 [hep-ex] (cit. on p. 2).

[54] ATLAS Collaboration, *Search for Higgs boson pair production in the $\gamma\gamma WW^*$ channel using pp collision data recorded at $\sqrt{s} = 13$ TeV with the ATLAS detector*, Eur. Phys. J. C **78** (2018) 1007, arXiv: 1807.08567 [hep-ex] (cit. on p. 2).

[55] ATLAS Collaboration, *Search for Higgs boson pair production in the $WW^{(*)}WW^{(*)}$ decay channel using ATLAS data recorded at $\sqrt{s} = 13$ TeV*, JHEP **05** (2019) 124, arXiv: 1811.11028 [hep-ex] (cit. on p. 2).

[56] CMS Collaboration, *Search for nonresonant Higgs boson pair production in the four leptons plus two b jets final state in proton–proton collisions at $\sqrt{s} = 13$ TeV*, JHEP **06** (2023) 130, arXiv: 2206.10657 [hep-ex] (cit. on p. 2).

[57] ATLAS Collaboration, *Search for non-resonant Higgs boson pair production in the $2b + 2\ell + E_T^{miss}$ final state in pp collisions at $\sqrt{s} = 13$TeV with the ATLAS detector*, JHEP **02** (2024) 037, arXiv: 2310.11286 [hep-ex] (cit. on p. 2).

[58] ATLAS Collaboration, *Combination of searches for Higgs boson pairs in pp collisions at $\sqrt{s} = 13$ TeV with the ATLAS detector*, Phys. Lett. B **800** (2020) 135103, arXiv: 1906.02025 [hep-ex] (cit. on p. 2).

[59] ATLAS Collaboration, *Constraints on the Higgs boson self-coupling from single- and double-Higgs production with the ATLAS detector using pp collisions at $\sqrt{s} = 13$ TeV*, Phys. Lett. B **843** (2023) 137745, arXiv: 2211.01216 [hep-ex] (cit. on p. 2).

[60] A. Djouadi, J. Kalinowski, and M. Spira, *HDECAY: A program for Higgs boson decays in the Standard Model and its supersymmetric extension*, Comput. Phys. Commun. **108** (1998) 56, arXiv: hep-ph/9704448 (cit. on p. 2).

[61] ATLAS Collaboration, *Identification of Boosted Higgs Bosons Decaying Into $b\bar{b}$ With Neural Networks and Variable Radius Subjets in ATLAS*, ATL-PHYS-PUB-2020-019, 2020, URL: https://cds.cern.ch/record/2724739 (cit. on pp. 2, 5).

[62] ATLAS Collaboration, *Efficiency corrections for a tagger for boosted $H \to b\bar{b}$ decays in pp collisions at $\sqrt{s} = 13$ TeV with the ATLAS detector*, ATL-PHYS-PUB-2021-035, 2021, URL: https://cds.cern.ch/record/2777811 (cit. on pp. 2, 5, 9).

[63] ATLAS Collaboration, *The ATLAS Collaboration Software and Firmware*, ATL-SOFT-PUB-2021-001, 2021, URL: https://cds.cern.ch/record/2767187 (cit. on p. 4).

[64] ATLAS Collaboration, *Luminosity determination in pp collisions at $\sqrt{s} = 13$ TeV using the ATLAS detector at the LHC*, Eur. Phys. J. C **83** (2023) 982, arXiv: 2212.09379 [hep-ex] (cit. on p. 4).

[65] ATLAS Collaboration, *ATLAS data quality operations and performance for 2015–2018 data-taking*, JINST **15** (2020) P04003, arXiv: 1911.04632 [physics.ins-det] (cit. on p. 4).

[66] G. Avoni et al., *The new LUCID-2 detector for luminosity measurement and monitoring in ATLAS*, JINST **13** (2018) P07017 (cit. on p. 4).

[67] ATLAS Collaboration, *The ATLAS Simulation Infrastructure*, Eur. Phys. J. C **70** (2010) 823, arXiv: 1005.4568 [physics.ins-det] (cit. on p. 4).

[68] S. Agostinelli et al., *GEANT4 – a simulation toolkit*, Nucl. Instrum. Meth. A **506** (2003) 250 (cit. on p. 4).

[69] J. Alwall et al., *The automated computation of tree-level and next-to-leading order differential cross sections, and their matching to parton shower simulations*, JHEP **07** (2014) 079, arXiv: 1405.0301 [hep-ph] (cit. on pp. 4, 5).

[70] NNPDF Collaboration, *Parton distributions for the LHC run II*, JHEP **04** (2015) 040, arXiv: 1410.8849 [hep-ph] (cit. on p. 4).

[71] P. Nason, *A new method for combining NLO QCD with shower Monte Carlo algorithms*, JHEP **11** (2004) 040, arXiv: hep-ph/0409146 (cit. on p. 5).

[72] S. Frixione, P. Nason, and C. Oleari, *Matching NLO QCD computations with parton shower simulations: the POWHEG method*, JHEP **11** (2007) 070, arXiv: 0709.2092 [hep-ph] (cit. on p. 5).

[73] S. Alioli, P. Nason, C. Oleari, and E. Re, *A general framework for implementing NLO calculations in shower Monte Carlo programs: the POWHEG BOX*, JHEP **06** (2010) 043, arXiv: 1002.2581 [hep-ph] (cit. on p. 5).

[74] J. Butterworth et al., *PDF4LHC recommendations for LHC Run II*, J. Phys. G **43** (2016) 023001, arXiv: 1510.03865 [hep-ph] (cit. on p. 5).

[75] ATLAS Collaboration, *Validation of signal Monte Carlo event generation in searches for Higgs boson pairs with the ATLAS detector*, ATL-PHYS-PUB-2019-007, 2019, URL: https://cds.cern.ch/record/2665057 (cit. on p. 5).

[76] NNPDF Collaboration, *Parton distributions with LHC data*, Nucl. Phys. B **867** (2013) 244, arXiv: 1207.1303 [hep-ph] (cit. on p. 5).

[77] R. Contino, D. Pappadopulo, D. Marzocca, and R. Rattazzi, *On the effect of resonances in composite Higgs phenomenology*, JHEP **10**, 81 (2011) 81, arXiv: 1109.1570 [hep-ph] (cit. on pp. 5, 13).

[78] T. Sjöstrand et al., *An introduction to PYTHIA 8.2*, Comput. Phys. Commun. **191** (2015) 159, arXiv: 1410.3012 [hep-ph] (cit. on p. 5).

[79] ATLAS Collaboration, *ATLAS Pythia 8 tunes to 7 TeV data*, ATL-PHYS-PUB-2014-021, 2014, URL: https://cds.cern.ch/record/1966419 (cit. on p. 5).

[80] D. J. Lange, *The EvtGen particle decay simulation package*, Nucl. Instrum. Meth. A **462** (2001) 152 (cit. on p. 5).

[81] ATLAS Collaboration, *The Pythia 8 A3 tune description of ATLAS minimum bias and inelastic measurements incorporating the Donnachie–Landshoff diffractive model*, ATL-PHYS-PUB-2016-017, 2016, URL: https://cds.cern.ch/record/2206965 (cit. on p. 5).

[82] ATLAS Collaboration, *Performance of the ATLAS trigger system in 2015*, Eur. Phys. J. C **77** (2017) 317, arXiv: 1611.09661 [hep-ex] (cit. on p. 5).

[83] ATLAS Collaboration, *Trigger Menu in 2018*, ATL-DAQ-PUB-2019-001, 2019, URL: https://cds.cern.ch/record/2693402 (cit. on p. 5).

[84] ATLAS Collaboration, *Performance of the ATLAS Level-1 topological trigger in Run 2*, Eur. Phys. J. C **82** (2022) 7, arXiv: 2105.01416 [hep-ex] (cit. on p. 5).

[85] M. Cacciari, G. P. Salam, and G. Soyez, *The anti-k_t jet clustering algorithm*, JHEP **04** (2008) 063, arXiv: 0802.1189 [hep-ph] (cit. on p. 5).

[86] M. Cacciari, G. P. Salam, and G. Soyez, *FastJet user manual*, Eur. Phys. J. C **72** (2012) 1896, arXiv: 1111.6097 [hep-ph] (cit. on p. 5).

[87] ATLAS Collaboration, *Topological cell clustering in the ATLAS calorimeters and its performance in LHC Run 1*, Eur. Phys. J. C **77** (2017) 490, arXiv: 1603.02934 [hep-ex] (cit. on p. 5).

[88] D. Krohn, J. Thaler, and L.-T. Wang, *Jet trimming*, JHEP **02** (2010) 084, arXiv: 0912.1342 [hep-ph] (cit. on p. 5).

[89] ATLAS Collaboration, *Optimisation of large-radius jet reconstruction for the ATLAS detector in 13 TeV proton–proton collisions*, Eur. Phys. J. C **81** (2021) 334, arXiv: 2009.04986 [hep-ex] (cit. on p. 5).

[90] ATLAS Collaboration, *Jet mass reconstruction with the ATLAS Detector in early Run 2 data*, ATLAS-CONF-2016-035, 2016, URL: https://cds.cern.ch/record/2200211 (cit. on p. 5).

[91] ATLAS Collaboration, *Jet reconstruction and performance using particle flow with the ATLAS Detector*, Eur. Phys. J. C **77** (2017) 466, arXiv: 1703.10485 [hep-ex] (cit. on p. 5).

[92] ATLAS Collaboration, *Performance of pile-up mitigation techniques for jets in pp collisions at $\sqrt{s} = 8$ TeV using the ATLAS detector*, Eur. Phys. J. C **76** (2016) 581, arXiv: 1510.03823 [hep-ex] (cit. on p. 5).

[93] ATLAS Collaboration, *Jet energy scale and resolution measured in proton–proton collisions at $\sqrt{s} = 13$ TeV with the ATLAS detector*, Eur. Phys. J. C **81** (2021) 689, arXiv: 2007.02645 [hep-ex] (cit. on pp. 6, 9).

[94] T. Chen and C. Guestrin, "XGBoost: A Scalable Tree Boosting System", *Proceedings of the 22nd ACM SIGKDD International Conference on Knowledge Discovery and Data Mining*, KDD '16, San Francisco, California, USA: ACM, 2016 785, ISBN: 978-1-4503-4232-2, URL: http://doi.acm.org/10.1145/2939672.2939785 (cit. on p. 8).

[95] P. Baldi, K. Cranmer, T. Faucett, P. Sadowski, and D. Whiteson, *Parameterized neural networks for high-energy physics*, Eur. Phys. J. C **76** (2016), arXiv: 1601.07913 [hep-ex], URL: https://doi.org/10.1140/epjc/s10052-016-4099-4 (cit. on p. 8).

[96] ATLAS Collaboration, *In situ calibration of large-radius jet energy and mass in 13 TeV proton–proton collisions with the ATLAS detector*, Eur. Phys. J. C **79** (2019) 135, arXiv: 1807.09477 [hep-ex] (cit. on p. 9).

[97] ATLAS Collaboration, *Measurement of the ATLAS Detector Jet Mass Response using Forward Folding with $80\,fb^{-1}$ of $\sqrt{s} = 13$ TeV pp data*, ATLAS-CONF-2020-022, 2020, URL: https://cds.cern.ch/record/2724442 (cit. on p. 9).

[98] ATLAS Collaboration, *Jet energy scale measurements and their systematic uncertainties in proton–proton collisions at $\sqrt{s} = 13$ TeV with the ATLAS detector*, Phys. Rev. D **96** (2017) 072002, arXiv: 1703.09665 [hep-ex] (cit. on p. 9).

[99] ATLAS Collaboration, *Measurements of WH and ZH production in the $H \to b\bar{b}$ decay channel in pp collisions at 13 TeV with the ATLAS detector*, Eur. Phys. J. C **81** (2021) 178, arXiv: 2007.02873 [hep-ex] (cit. on p. 9).

[100] G. Cowan, K. Cranmer, E. Gross, and O. Vitells, *Asymptotic formulae for likelihood-based tests of new physics*, Eur. Phys. J. C **71** (2011) 1554, arXiv: 1007.1727 [physics.data-an] (cit. on p. 10), Erratum: Eur. Phys. J. C **73** (2013) 2501.

[101] A. L. Read, *Presentation of search results: the CL_S technique*, J. Phys. G **28** (2002) 2693 (cit. on p. 10).